Aerosol from the Asian monsoon ubiquitous throughout the extratropical stratosphere

Franziska Köllner[1,2], Matthias Kohl[2], Fatih Ekinci[1,2], Oliver Eppers[2], Johannes Schneider[2], Antonis Dragoneas[2], Sergej Molleker[2], Sören Johansson[3], Jörn Ungermann[4], Erik Kretschmer[3], Michael Höpfner[3], Valentin Lauther[5], C. Michael Volk[5], Oliver Appel[1,2], Philipp Brauner[2], Daniel Kunkel[1], Hans-Christoph Lachnitt[1], Heiko Bozem[1], Franziska Weyland[1], Nicolas Emig[1], Linda Ort[2], Andreas Zahn[3], Laura Tomsche[1,6], Andrea Pozzer[2,7], Jos Lelieveld[2,7], Yafang Cheng[2], Martin Riese[4,5], Peter Hoor[1], and Stephan Borrmann[1,2]

[1]Johannes Gutenberg University, Institute for Atmospheric Physics, Mainz, 55128, Germany
[2]Max Planck Institute for Chemistry, Mainz, 55128, Germany
[3]Karlsruhe Institute of Technology, Institute of Meteorology and Climate Research – Atmospheric Trace Gases and Remote Sensing (IMK-ASF), 76021, Karlsruhe, Germany
[4]Forschungszentrum Jülich, Institute of Climate and Energy Systems – Stratosphere (ICE-4), 52428, Jülich, Germany
[5]University of Wuppertal, Institute for Atmospheric and Environmental Research, 42119, Wuppertal, Germany
[6]German Aerospace Center, 82234 Weßling, Germany
[7]The Cyprus Institute, Climate and Atmosphere Research Center, 2121, Nicosia, Cyprus

This manuscript is a non-peer reviewed preprint that has been submitted for consideration in the Journal Nature Communications Earth and Environment.

Aerosol from the Asian monsoon ubiquitous throughout the extratropical stratosphere

Franziska Köllner[1,2], Matthias Kohl[2], Fatih Ekinci[1], Oliver Eppers[2], Johannes Schneider[2], Antonis Dragoneas[2], Sergej Molleker[2], Sören Johansson[3], Jörn Ungermann[4], Erik Kretschmer[3], Michael Höpfner[3], Valentin Lauther[5], C. Michael Volk[5], Oliver Appel[1,2], Philipp Brauner[2], Daniel Kunkel[1], Hans-Christoph Lachnitt[1], Heiko Bozem[1], Franziska Weyland[1], Nicolas Emig[1], Linda Ort[2], Andreas Zahn[3], Laura Tomsche[1,6], Andrea Pozzer[2,7], Jos Lelieveld[2,7], Yafang Cheng[2], Martin Riese[4,5], Peter Hoor[1], and Stephan Borrmann[1,2]

[1]Johannes Gutenberg University, Institute for Atmospheric Physics, Mainz, 55128, Germany
[2]Max Planck Institute for Chemistry, Mainz, 55128, Germany
[3]Karlsruhe Institute of Technology, Institute of Meteorology and Climate Research – Atmospheric Trace Gases and Remote Sensing (IMK-ASF), 76021, Karlsruhe, Germany
[4]Forschungszentrum Jülich, Institute of Climate and Energy Systems – Stratosphere (ICE-4), 52428, Jülich, Germany
[5]University of Wuppertal, Institute for Atmospheric and Environmental Research, 42119, Wuppertal, Germany
[6]German Aerospace Center, 82234 Weßling, Germany
[7]The Cyprus Institute, Climate and Atmosphere Research Center, 2121, Nicosia, Cyprus
[*]f.koellner@mpic.de

ABSTRACT

Asian summer monsoon (ASM) convection efficiently transports surface emissions into the upper troposphere, leading to the formation of the Asian tropopause aerosol layer (ATAL). The ATAL can affect Earth's climate directly by scattering solar radiation and indirectly by cloud formation. Little is known about the global distribution of aerosol originating in the ASM, particularly in the extratropical tropopause region, where the climate is sensitive to anthropogenic perturbations. Here, we present airborne aerosol composition measurements in the ASM outflow region over the North Pacific. Our analysis demonstrates the important seasonal aerosol transport from Asia into the northern lower stratosphere. Particulate ammonium nitrate and organic compounds are ubiquitous in the stratosphere with a mass concentration of up to 1 µg m^{-3}. This is the first detection of ammonium nitrate in the stratosphere outside the monsoon region. Together with the results from a global chemistry-climate model, we find that this northward transport of Asian aerosol is persistent from July to September, recurring yearly. The simulations suggest that particulate ammonium persists for several months, significantly affecting aerosol acidity in the lower stratosphere. This highlights the widespread impact of Asian emissions on stratospheric aerosol, with implications for ozone chemistry and the atmospheric radiation budget.

Introduction

Early studies of stratospheric aerosol primarily focused on the Junge layer[1,2], characterized by its altitude (15 to 25 km), broad latitudinal extent, and composition. The main constituent is sulfuric acid aerosol formed from natural sources such as volcanic eruptions and the tropical injection of carbonyl sulfide. However, recent satellite and balloon-borne observations have identified the existence of another aerosol layer at altitudes of 13 to 18 km, known as the Asian Tropopause Aerosol Layer (ATAL)[3–5]. The ATAL predominantly affects regions from the eastern Mediterranean (southward to North Africa) to eastern China (southward to Thailand) every year from June to September. Its main components are ammonium nitrate- and organic-containing aerosol[6–10]. The Asian summer monsoon (ASM) plays a significant role in the formation and maintenance of the ATAL by rapidly transporting aerosol precursor gases from the Asian boundary layer into the upper troposphere. Further, precipitation by monsoon convective clouds efficiently washes out pre-existing aerosol particles, leading to a weak condensation sink in the outflow of the monsoon[11]. Subsequently, the isolated motion within the ASM anticyclone is favourable for new particle formation and particle growth, driving the formation of the ATAL[10,12,13] (Extended Data Fig. 5).

Although the ATAL has a significant regional influence on the composition and abundance of aerosol in the upper troposphere and lower stratosphere (UTLS), along with strong radiative and climatic effects[5], there remains a lack of experimental

evidence on its broader impact across the Northern hemisphere. Recent modelling studies proposed that the ATAL contributes significantly to the aerosol concentration and composition in the Northern hemispheric stratosphere outside the monsoon region[14,15]. Even in remote Arctic regions, lidar measurements detected the influence of the ASM on stratospheric aerosol[16]. A better understanding of the potential perturbation of stratospheric aerosol by the ASM is crucial for reliably analysing ozone trends[17,18] and climate radiative forcings[19–21]. In this study, we provide in-situ and remote sensing measurements as well as global chemistry-climate model simulations of aerosol chemical properties in the extratropical lower stratosphere (ExLS) towards the end of the monsoon season, exploring sources, transport pathways, and the persistence of these aerosol particles.

Results and Discussion

Aircraft-based aerosol composition measurements in the extratropical UTLS in summer and autumn

The PHILEAS aircraft-based mission (Probing High Latitude Export of Air from the Asian Summer Monsoon) studied the export of ASM air into the extratropical UTLS. The main part of the mission took place in August and September 2023 out of Anchorage, Alaska (Extended Data Fig. 6). The research aircraft was equipped with a comprehensive suite of in-situ and remote-sensing instruments for aerosol and gas analysis. We obtained vertically-resolved submicron aerosol composition measurements (particle diameter > 110 nm) up to an altitude of 15 km or a potential temperature (Theta) of 410 K using the ERICA instrument[7,22] (ERC Instrument for the Chemical composition of Aerosols). The ERICA Aerosol Mass Spectrometer (ERICA-AMS) is based on thermal desorption with subsequent electron-impact ionization, providing in-situ real-time mass concentrations of particulate organics, nitrate, sulfate, and ammonium (Methods). We categorized the measured air masses into "polluted" and "undisturbed stratosphere" based on the following criteria. Methane (CH_4) and dichloromethane (CH_2Cl_2) served as pollution tracers for Asian emissions[23–27]. The air mass is referred to as "polluted" if these tracers are elevated. In contrast, the undisturbed stratospheric air is characterized by low values of CH_4 and CH_2Cl_2, along with nitrous oxide (N_2O) mixing ratios below the tropospheric mean value. For this study, we excluded data that were obtained during sampling in air masses that were influenced by biomass burning events outside the monsoon region. More detailed information about the methods can be found in the Methods Section.

Figure 1a illustrates the vertically-resolved aerosol composition measurements obtained during all PHILEAS flights over the North Pacific and Alaska region in August/September 2023, using potential temperature as the vertical coordinate. The two types of air masses exhibit differences in aerosol mass concentrations and composition. The undisturbed stratospheric air is characterized by very low concentrations of ammonium, nitrate, and organic aerosol, close to the detection limit (Supplementary Fig. S1), while sulfate being the main constituent. In contrast, polluted air shows a significant increase in the concentrations of all aerosol species with increasing potential temperature above 360 K. Nitrate mass concentrations can reach values of up to approximately 0.4 $\mu g\,m^{-3}$. Similarly, concentrations of ammonium and organic aerosol can reach maximum values of about 0.2 $\mu g\,m^{-3}$ and 0.3 $\mu g\,m^{-3}$, respectively. Figure 1b presents concurrent measurements from the airborne infrared limb-imaging instrument GLORIA. The timeseries from an exemplary flight on 1 September 2023 demonstrates the unambiguous existence of ammonium nitrate (AN) particles in the UTLS region[6]. The analysis of the GLORIA infrared spectra, compared with laboratory measurements, further reveals that these particles are in solid phase (Extended Data Fig. 7). This is consistent with prior observations inside the ASM anticyclone[6]. Together, the abundance of solid AN and organic aerosol in the extratropical UTLS during summer and autumn is controlled by pollution events associated with increased CH_4 and CH_2Cl_2 mixing ratios.

Assessing the role of transport from the Asian summer monsoon on aerosol composition in the extratropical stratosphere

To investigate the sources and mechanisms responsible for transporting this type of polluted air masses into the extratropics, we utilized ECMWF reanalysis data (ERA5) (Methods). Additionally, global-scale simulations using the ECHAM/MESSy Atmospheric Chemistry model (EMAC)[28] were conducted to gain further insights into the origin of the pollution aerosol (Methods). Figure 2 illustrates the measured mass concentrations of nitrate, ammonium, and organic aerosol in polluted air, as a function of potential temperature and equivalent latitude. The highest aerosol concentrations were observed above the 8 PVU isoline, suggesting a stratospheric signature of the air[29]. Along with this, N_2O mixing ratios were found to be below the tropospheric mean value of 337 ppb (Fig. 2) and ozone above 100 ppb (not shown). Thus, the polluted air masses with AN and organic aerosol were clearly detected in the ExLS.

We have evidence that the observed pollution originates from Asian sources in combination with the Asian summer monsoon circulation. First, the increase of AN and organic aerosol in the ExLS is associated with elevated mixing ratios of CH_4 and CH_2Cl_2 (Fig. 1 and Methods). Previous studies have identified Asia as the main contributor to global emissions of CH_4[25] and CH_2Cl_2[26,30]. Second, the EMAC reference simulation of ammonium and nitrate concentrations in Fig. 3a and c demonstrates the northward transport of aerosol from the subtropical Asian region into the extratropics. Along with this, we performed a

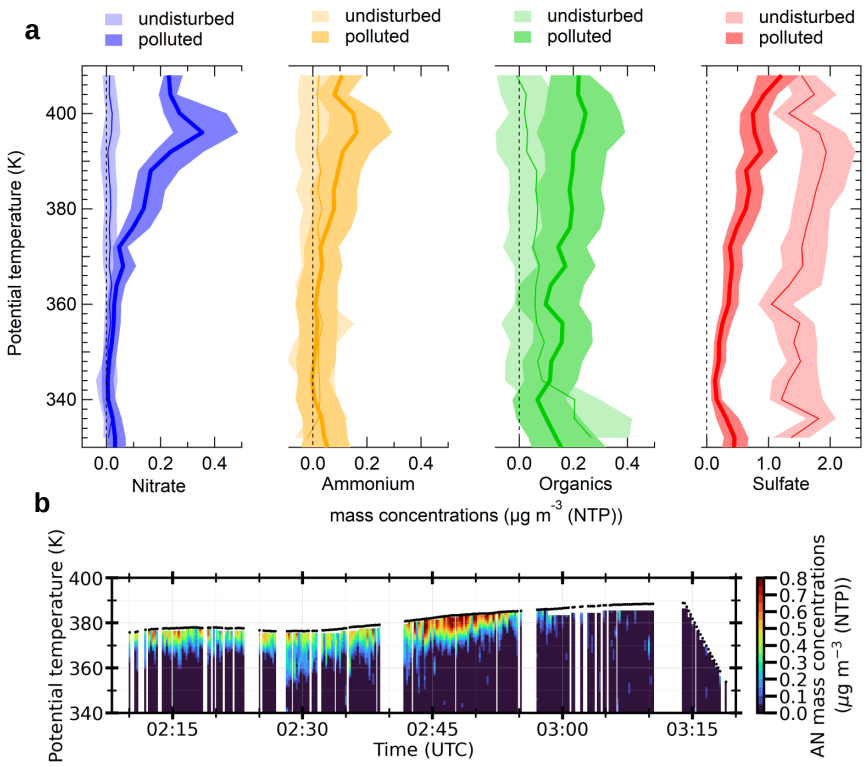

Figure 1. UTLS aerosol composition measured during all PHILEAS flights over the North Pacific and Alaska region. **a,** ERICA-AMS mass concentrations of particulate nitrate (blue), ammonium (orange), organics (green), and sulfate (red) as a function of potential temperature. The thick lines and the shaded areas represent the medians and interquartile ranges, respectively, in the corresponding potential temperature bin. Data associated with undisturbed stratospheric and polluted air are given in lighter and darker colours, respectively. **b,** Airborne limb-imaging observations by GLORIA of ammonium nitrate (AN) concentration (coloured) as potential temperature projections measured during the PHILEAS flight on 1-2 September 2023.

sensitivity simulation with EMAC to assess the role of Asian emissions on the presence of ammonium in the ExLS in summer and autumn. Therefore, all anthropogenic emissions of aerosol precursor gases, including ammonia, nitrogen oxides, and sulfur dioxide, from South-East Asia were excluded (Supplementary Fig. S3). By comparing the two simulations in Fig. 3b, it is illustrated that the abundance of AN from the subtropics to the extratropics is highly sensitive to the availability of ammonia from Asia. The highest modeled concentrations of AN, particularly during the Northern hemispheric summer and autumn, are almost exclusively attributable to increased availability of ammonia from Asian sources. This is in line with the findings of Xenofontos et al.[10], who showed the importance of ammonia for the formation of the ATAL. So far, our in-situ observations, combined with EMAC modelling, demonstrate for the first time the significant influence of Asian boundary layer emissions on the widespread distribution of AN and organic aerosol in the northern lower stratosphere.

We examined the key processes responsible for the long-range transport of aerosol from Asia into the ExLS. Initially, the ATAL is formed through gas-to-particle conversion, specifically through new particle formation and particle growth, between 355 and 380 K during summer, as reported in previous studies[7,12,13] (Extended Data Fig. 5). The slow diabatic uplift within the isolated ASM anticyclone, requiring time scales of weeks[31,32], is crucial for the observed increase in aerosol mass (Extended Data Fig. 5). Correspondingly, EMAC simulations in August/September 2023 (Fig. 3d) illustrate the ATAL, characterized by enhanced aerosol mass over Asia in the upper region of the ASM anticyclone between 360 K and 420 K (Theta). Regarding the subsequent northward transport, our measurements show that concentrations of AN and organic aerosol decrease with increasing equivalent latitudes on isentropic levels above 370 K (Fig. 2). In contrast, the concentrations are low in the vicinity of the subtropical jet (40-50° N and 2-8 PVU), suggesting that the transport into the ExLS across the subtropical jet plays a minor role for the observed aerosol distribution. We can thus conclude that the widespread abundance of AN and organic aerosol in the northern lower stratosphere is linked to both the ASM circulation and subsequent distribution by quasi-horizontal advection

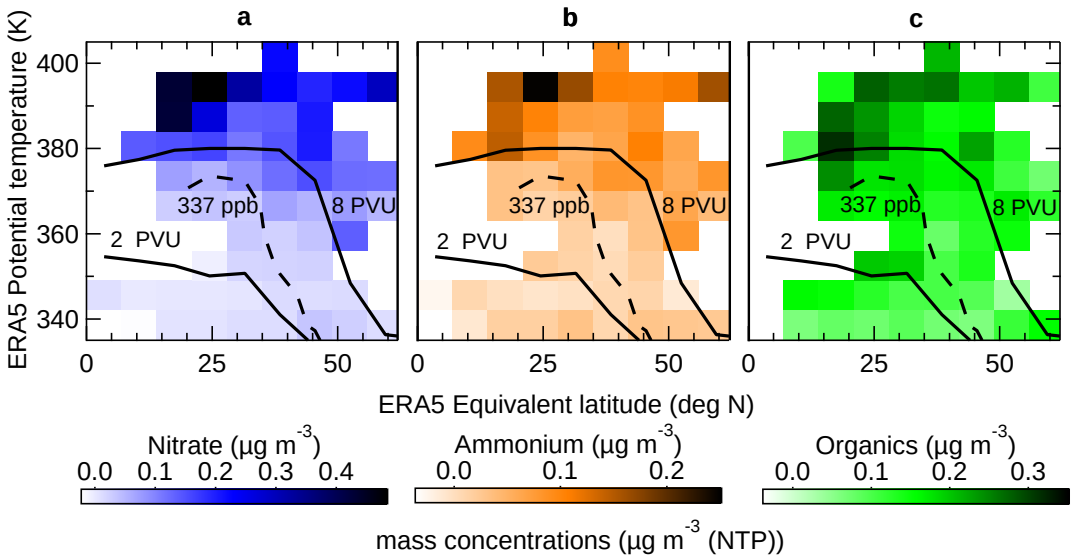

Figure 2. Spatially and vertically resolved aerosol composition during all PHILEAS flights over the North Pacific and Alaska region. ERICA-AMS mass concentrations of **a,** particulate nitrate (blue), **b,** ammonium (orange), and **c,** organics (green) as a function of ERA5-derived potential temperature and equivalent latitude. Data are associated with polluted air masses from Asia. Colours show median values for each grid cell. The black solid lines represent the 2 and 8 PVU isolines in the corresponding equivalent latitude bin. The black dashed line shows the isoline of N_2O at 337 ppb.

and mixing in the stratosphere, in particular above 370 K (Theta) (Extended Data Fig. 5). Consistent with this interpretation, EMAC model simulations in August and September 2023 also indicate that the northward transport of aerosol from the ASM follows isentropes into the ExLS (Fig. 3d). The irreversible mixing process is evidenced by intermediate mixing lines between the tropospheric (high N_2O) and stratospheric (low N_2O) regimes, along with higher nitrate concentrations (Extended Data Fig. 8).

Persistence of ammonium nitrate in the stratosphere using global-chemistry modelling

To further assess the persistence of particulate AN in the stratosphere over an extended period, we performed global-scale simulations using the EMAC model from January 2021 to March 2024 (Fig. 3a-c). The simulations reveal that ammonium and nitrate concentrations show a seasonal pattern, albeit differing in strength. Ammonium concentrations in the ExLS gradually decrease over the months, forming a background ammonium layer that remains visible until the onset of the next monsoon season (Fig. 3a). By the end of the year, the ammonium layer in the northern latitudes descends into the region of 8 PVU (Figs. 3e,f). In contrast, nitrate has a shorter lifetime in the stratosphere compared to ammonium, returning to background concentrations by the end of the year (Fig. 3c). The simulations also indicate that a diminishing nitrate abundance in the stratosphere is accompanied by an increase in bisulfate (Fig. 3g).

We thus hypothesize that particulate ammonium nitrate is replaced by ammonium (bi-)sulfate, suggesting that chemical processes, rather than transport processes, cause the varying abundance and residence time of ammonium and nitrate on both seasonal and annual scales. The process can be explained as follows. Ammonium nitrate forms only under ammonia-rich conditions, where sulfate is fully neutralized by ammonium, with excess ammonia available[33]. However, in the stratosphere, sulfuric acid is the main constituent, favouring the formation of ammonium (bi-)sulfate because sulfuric acid is a stronger acid compared to nitric acid. In the transition from ammonia-rich to ammonia-poor conditions, ammonium bisulfate forms, as shown in Fig. 3g. Sulfuric acid can incorporate into AN particles through coagulation or condensation. Coagulation is slow in the unperturbed stratosphere[34], while condensation of sulfuric acid occurs only after significant sulfur emissions (e.g., volcanic eruptions) due to the low volatility of sulfuric acid. EMAC employs the thermodynamic equilibrium model, ISORROPIA-II[35], along with internally mixed aerosol modes. Here, AN is rapidly replaced by ammonium sulfate when it encounters sulfur-rich stratospheric air within the same grid box, establishing a new equilibrium. Consequently, the model might overestimate the rate at which nitrate is replaced by sulfate. Nevertheless, our preceding analysis demonstrates that ammonium resides in the particle phase as a neutralizing agent for the highly acidic stratospheric background environment. Meanwhile, particulate nitrate is depleted over time due to mixing with sulfate-rich stratospheric air. The rate of this process in the stratosphere remains an open

research question and cannot be inferred solely by thermodynamic equilibrium models.

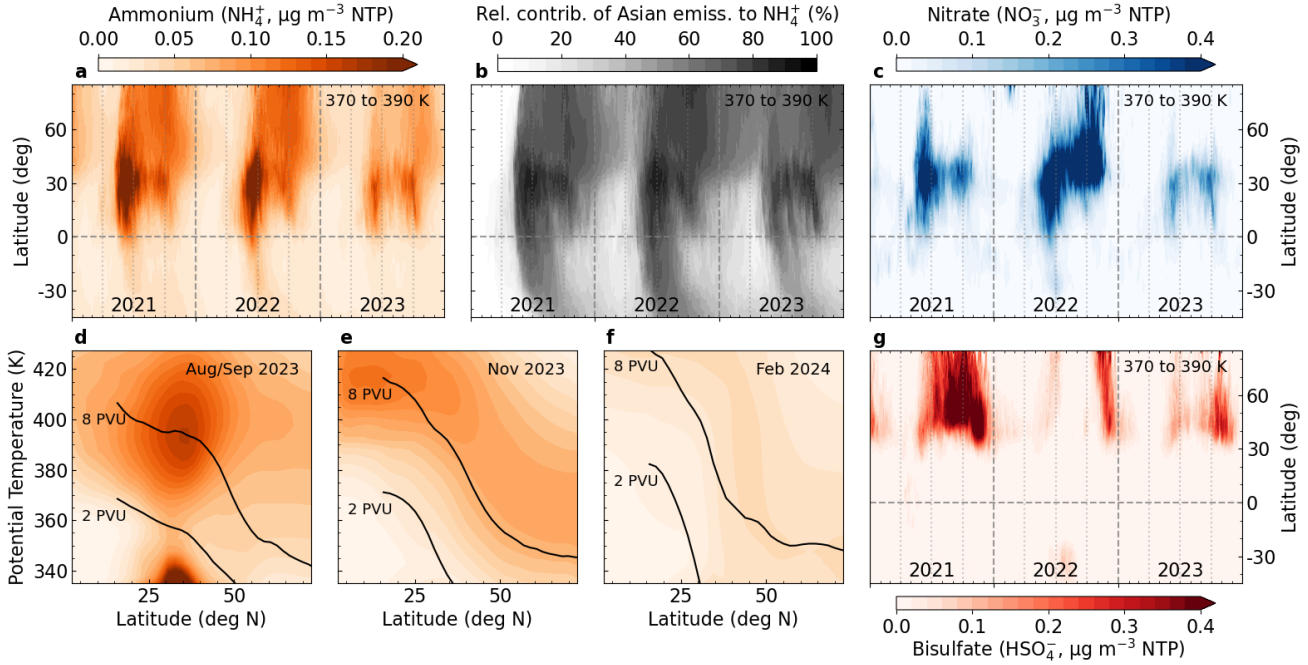

Figure 3. Simulated UTLS aerosol concentrations using the EMAC model. a,c,g, Zonally (global) and vertically (between 370 and 390 K in potential temperature) averaged concentrations of ammonium (a), nitrate (c) and bisulfate (g) from EMAC simulations as a function of latitude and time for the period of 2021-2023. **b,** Difference in ammonium concentrations between the reference simulation and a simulation without anthropogenic emissions from South and East Asia, revealing the ASM contribution to the UTLS ammonium concentrations. **d-f,** Zonally (75°E to 135°W) and monthly averaged profiles of ammonium concentrations at different stages of the evolution of ASM aerosol in the UTLS: During the PHILEAS mission from Mid-August to Mid-September 2023 (d), in November 2023 (e), and in February 2024 (f). Potential temperature is used as a vertical coordinate and the black lines represent the 2 PVU and 8 PVU isolines.

The simulations further reveal that the northward transport of aerosol originating from the ASM into the ExLS occurs annually during summer and autumn, albeit differing in strengths from year-to-year. The low concentrations observed in 2023 (Fig. 3a,c) can be attributed to two combined effects. First, the simulations indicate that less AN was formed locally in the ATAL, particularly during the early 2023 ASM season, compared to 2021 and 2022 (Supplementary Fig. S4). This anomaly might be due to an El-Niño-induced change in the ASM circulation[27,36]. Second, increased volcanic activity in 2023, similar to 2021 (Supplementary Fig. S4), resulted in additional sulfur in the stratosphere.

Atmospheric implications

This study highlights the significant impact of the ASM on aerosol composition and the state of aerosol neutralization in the ExLS. The introduction of ammonium as a neutralizing agent can modify the highly acidic stratospheric composition, dominated by sulfuric acid particles. Figure 4 compares the measured ammonium mass concentration with the calculated ammonium required for neutralization under the two scenarios: undisturbed stratospheric air and stratospheric air influenced by the ASM. Data points above the one-to-one line indicate non-neutralized aerosol. Our findings reveal that stratospheric aerosol associated with the ASM is on average neutralized, whereas the undisturbed stratospheric aerosol remains acidic. The ASM air contains higher ammonium and relatively low sulfate loadings compared to the undisturbed stratospheric air.

This study further explored the role of the ASM in transporting organic aerosol into the ExLS (Figs. 1-2). Previous research has shown that organic compounds constitute a significant portion of aerosol mass in the lower stratosphere, often linked to wildfires[21,37,38] or convection over regions like the Amazon basin[39–41]. However, unlike the sporadic injections of aerosol from wildfires, the EMAC simulations from 2021 to 2023 indicate a consistent northward transport of aerosol from

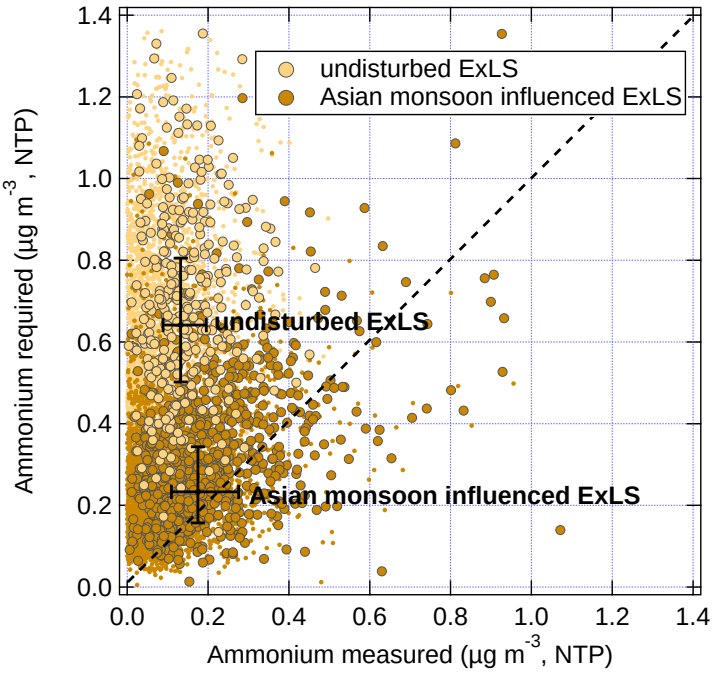

Figure 4. The influence of the ASM on aerosol composition and the state of aerosol neutralization in the ExLS. The graph shows the measured ammonium concentrations and the ammonium required for neutralization (Methods). Lighter and darker brownish colours show data points associated with undisturbed and Asian monsoon influenced stratospheric air, respectively. Measurements were taken in the extratropical lower stratosphere (ExLS), according to N_2O mixing ratios below 337 ppb. Data points are pre-filtered according to the NH_4 detection limits, shown by larger circles. Crosses demonstrate the median and interquartile ranges for the respective air masses, based on the pre-filtered data points. The dashed line shows the 1:1 line.

the ASM region from July to September each year (Fig. 3a,c). As a consequence, the presence of particulate ammonium and organic compounds in the stratosphere can significantly impact heterogeneous chemistry[17,18,42–44]. Previous studies have indicated that certain heterogeneous halogen-activation reactions are catalyzed by acids[45]. Consequently, changes in aerosol acidity might slow down ozone depletion processes. Conversely, recent findings suggest that oxidized organics can enhance the solubility of hydrochloric acid and increase heterogeneous reaction rates at relatively warm stratospheric temperatures[46]. This, in turn, promotes the activation of chlorine species and accelerates ozone loss. Thus, several effects on heterogeneous chemistry play a role, some of which may counterbalance each other. Certainly, the outflow of air from the ASM delivers significant amounts of short-lived chlorine species[23,27,42,47] and at the same time partially neutralized particles with organic content, as shown in this study. Moreover, these particles were found to be in a solid state, as shown by GLORIA data, and as such are crucial for heterogeneous chemistry[48–50] and cloud formation[51] in the UTLS region. Future studies should focus on the impact of these new aerosol constituents on stratospheric ozone depletion. Further investigation into the molecular structure and phase state (glassy or semi-liquid) of the organic aerosol is needed to better predict their influence on stratospheric chemistry.

The perturbation in stratospheric aerosol shown here can also impact global climate[20,21]. An earlier study indicated that the ATAL has exerted a short-term regional forcing of -0.1 $W\,m^{-2}$ since 1997, mainly due to efficient light scattering[5]. This cooling effect by the ATAL can locally mitigate the warming effect caused by the increase of greenhouse gases[19]. The value is comparable to the global forcing of greenhouse gases emitted in a similar period; however, the aerosol lifetime is much shorter compared to that of long-lived greenhouse gases. Moreover, the ASM is expected to become an increasing source of stratospheric aerosol in the coming decades, driven by rising emissions from the growing economies in Asia. This study has shown that the ASM provides an efficient yet overlooked pathway for the dispersion of AN and organic aerosol across the Northern Hemisphere. Thus, the ASM has a major potential to shift stratospheric aerosol composition and chemistry, thereby influencing ozone chemistry and global climate.

Methods

PHILEAS (Probing High Latitude Export of air from the Asian Summer Monsoon) aircraft-based mission. Airborne measurements of aerosol chemical properties, trace gases, and meteorological parameters were performed onboard the German research aircraft HALO (High Altitude and Long Range Research Aircraft). We successfully conducted 18 research flights of each 8-9 h (Extended Data Fig. 6). The mission was performed in three phases. The first phase (6 Aug - 21 Aug 2023) aimed to sample the extratropical stratospheric background air and the western flank of the ASM anticyclone above the Mediterranean Sea. Flights were conducted out of Oberpfaffenhofen, Germany. The second phase (26 Aug - 20 Sept 2023) was conducted out of Anchorage (Alaska), in order to measure filaments of the ASM anticyclone in the North Pacific region. The third phase (22 Sept - 27 Sept 2023) aimed to sample the altered stratospheric background air in autumn after the break-up of the ASM anticyclone. Flight tracks covered altitudes typically up to 15 km (Extended Data Fig. 6b) and potential temperature up to 410 K. In this study, we analyse data obtained during the second phase (26 Aug - 20 Sept 2023), thus, in the measurement region above the North Pacific, northern Canada, and Alaska (Extended Data Fig. 6a). As only measurements in the UTLS region are of interest for this study, we restricted the analysis to data obtained above 8 km altitude.

ERICA aerosol mass spectrometer. The ERICA (ERC Instrument for the Chemical composition of Aerosols) aerosol mass spectrometer was deployed to obtain vertically-resolved aerosol composition measurements up to 410 K potential temperature. The instrument is described in detail in Hünig et al.[22]. In brief, ambient sample air is supplied to ERICA by the HALO aerosol Submicrometer Inlet (HASI) (see Supplementary for details). Aerosol particles enter the instrument via a pressure-regulating critical orifice that maintains a constant mass flow into the instrument followed by an aerodynamic lens. The constant mass flow provides measurements at normal temperature and pressure (NTP, 20° C, 1013 hPa). Thus, in this study, all concentrations are given per normal cubicmeter. Further, two common methods for in situ real-time aerosol mass spectrometric analysis are integrated. First, the laser desorption ionization technique with subsequent time-of-flight mass spectrometry is adopted[52], obtaining mass spectral information of single particles. Single particle mass spectra of AN particles were inspected for the presence of sulfate. It was earlier shown that the abundance of AN in solid phase is facilitated by the internal mixing with small amounts of sulfuric acid[6]. Second, the thermal desorption with subsequent electron-impact ionization technique is implemented, similar to the Aerodyne aerosol mass spectrometer (AMS)[53,54]. The detectable particle size range by the ERICA-AMS is between 110 nm and 3.5 µm vacuum aerodynamic diameter, determined by the transmission efficiency of the aerodynamic lens. The detection limits of the ERICA-AMS are given in the Supplementary.

GLORIA remote sensing. The Gimballed Limb Observer for Radiance Imaging of the Atmosphere (GLORIA[55,56]) is an airborne limb-imaging Fourier Transform Spectrometer, which has been deployed during the PHILEAS campaign on the HALO aircraft to measure infrared limb-emission spectra of the atmosphere (spectral region: 750-1400 cm^{-1}, spectral sampling up to 0.0625 cm^{-1}). Radiometric calibration is performed using in-flight-measurements of two external blackbodies and upward viewing geometries. The level-1 processing is described by Kleinert et al.[57] and Ungermann et al.[58]. Atmospheric profiles of trace gases and aerosol, like solid ammonium nitrate, are retrieved from cloud top to flight altitudes. The general retrieval strategy is described by Johansson et al.[59] and Höpfner et al.[6]. Vertical resolutions of 600-800 m are achieved and uncertainties are estimated to about 30 %, mostly due to spectroscopic uncertainties.

UMAQS infrared absorption instrument. Transport tracers N_2O, CO, and CH_4 were measured with the University of Mainz Airborne Quantum cascade laser (QCL) Spectrometer (UMAQS). The instrument applies a multipath cell[60] providing an optical path of 76 m. Direct absorption of a QCL laser at 2200 cm^{-1} for N_2O and CO as well as 2990 cm^{-1} for CH_4 at a constant cell pressure of 40 Torr is used to determine the concentration of the absorbers, which are converted to mixing ratios using measured cell pressure and temperature. The instrument is in-situ calibrated against secondary gas standards of compressed dried ambient air, which are compared to standards from NOAA prior and after the campaign. With this setup, a total uncertainty (1 sigma) for the 1 Hz data set of 0.15 ppb_v for N_2O, 0.7 ppb_v for CO, and 0.8 ppb_v for CH_4 under in-flight conditions on straight legs was achieved.

HAGAR-V gas chromatograph and mass spectrometer. CH_2Cl_2 and C_2H_2 were measured in-situ by the five channel High Altitude Gas AnalyzeR (HAGAR-V) using gas chromatography (GC) and mass spectrometry (MS). The two GC channels of HAGAR-V's GC-MS module together provide a measurement every 120 s that has been integrated for 30 s. Frequent in-flight calibrations are performed using two working standard gases of compressed dried air. The working standards are calibrated at the University of Frankfurt based on AGAGE-derived calibrations according to the SIO-14 (CH_2Cl_2) and at the German weather service at Hohenpeißenberg based on NPL-derived calibrations according to the NPL12 scale (C_2H_2). During PHILEAS, the median in-flight precision was 1.3 % for CH_2Cl_2 and 2.5 % for C_2H_2. The quantity dDCM (delta dichloromethane) indicating

the excess CH_2Cl_2 due to Asian sources is derived from the CH_2Cl_2 and concurrent N_2O measurements as follows:

$$[\mathrm{dDCM}] = [\mathrm{CH_2Cl_2}] - [\mathrm{CH_2Cl_2(N_2O)}]_{\mathrm{clean}}. \quad (1)$$

The "clean" mixing ratio (last term) as a function of N_2O is derived from a fit to the CH_2Cl_2–N_2O relation including only the lowest 10 % of CH_2Cl_2 values in each N_2O bin.

ERA5 data. ERA5 (ECMWF Reanalysis v5) data were used with a horizontal grid spacing of 1° and a temporal resolution of 6 hours. The model has 137 vertical hybrid sigma-pressure levels from the surface up to 0.01 hPa with a vertical spacing of about 500 m in the UTLS[61]. The model data are linearly interpolated in space and time onto the flight path. For the calculation of the potential vorticity (PV) and the equivalent latitude, the native variables are interpolated on isentropic surfaces from 240 K up to 2000 K. To display trace gases in the UTLS, the equivalent latitude is used frequently[62]. It is characterized by a spherical-symmetrical area with equal distribution of isentropic PV contours centered around the poles. The respective latitude of a given pole-centred PV circle constitutes the equivalent latitude. Due to adiabatic PV-conservation, it allows to account for the reversible (adiabatic) part of transport.

EMAC global aerosol modelling. All global simulations were performed with the ECHAM/MESSy Atmospheric Chemistry model (EMAC)[28], combining the general circulation model ECHAM5 with the Modular Earth Submodel System (MESSy). We applied a spectral horizontal resolution of T63 (1.875° × 1.875°) and 90 vertical levels up to 0.1 hPa (approx. 80 km). The model's dynamics were weakly "nudged" towards reanalysis data[61]. Anthropogenic surface emissions of aerosol and reactive gases were sourced from the CEDS database[63] for the year 2019. Aerosol microphysics are treated with the submodel GMXe[64], based on 7 interactive lognormal modes (soluble nucleation, Aitken, accumulation and coarse mode as well as insoluble Aitken, accumulation and coarse mode). All particles are considered spherical and can transition between modes through coagulation, condensational growth, or evaporation after each timestep. Inorganic aerosol thermodynamics were calculated using ISORROPIA-II[35], while organic gas-aerosol partitioning is separately managed based on source and volatility. The model setup was evaluated using observations from the PHILEAS and StratoClim[7] campaigns (see Supplementary for details), showing that EMAC can reproduce the observed ammonium and nitrate enhancements in the UTLS, both in the source region and at higher latitudes.

CH_4 and CH_2Cl_2 to identify air masses associated with Asian sources. The ASM anticyclone shows higher values of tropospheric tracers, such as CH_4 and CH_2Cl_2, compared to regions outside of the anticyclone[23,24,27,65]. Methane can be related mainly to agricultural sources in Asia[25], whereas dichloromethane is largely emitted from anthropogenic activities in Asia[26,30]. Both trace gases were used to identify air masses associated with ASM and thus Asian sources. We combined the two data sets (Extended Data Fig. 9) in order to obtain certain thresholds for polluted (CH_4- and CH_2Cl_2-rich) and undisturbed stratospheric air (CH_4- and CH_2Cl_2-poor). As a result, we used a CH_4 threshold of 1860 ppb for undisturbed stratospheric air. In this range, dDCM shows values below 10 ppt, suggesting a significant influence of Asian anthropogenic sources on these air masses to be very unlikely. We further used a CH_4 threshold of 1920 ppb for polluted air. In this range, dDCM values are increasing and reaching values above 200 ppt, leading to the conclusion that these air masses are likely influenced by Asian anthropogenic sources.

CO and C_2H_2 to identify air masses associated with biomass burning. We further used measurements of acetylene (C_2H_2) and carbonmonoxide (CO) to identify air masses influenced by biomass burning (BB), which were sampled occasionally in the UTLS during the PHILEAS mission. A data point was associated with BB when C_2H_2 was above 80 ppt and CO above 40 ppb as well as dDCM below 20 ppt. The latter step was important as CO, C_2H_2, and CH_2Cl_2 have sources in Asia that are in close proximity to each other and a clear differentiation between Asian BB and Asian anthropogenic sources was not possible. Thus, the BB associated air masses only refer to regions outside Asia with a relatively low loading of CH_2Cl_2. We removed the data that can be attributed to BB outside of the ASM region because this is not an intended topic for this publication.

N_2O, O_3, and CH_4 for identifying stratospheric air and mixing processes. Trace gas measurements of N_2O and O_3 are considered to separate tropospheric and stratospheric air[66,67]. Nitrous oxide allows for an unambiguous identification of stratospheric air, because it is chemically inert in the troposphere, leading to an almost homogeneous vertical distribution in the troposphere. In the stratosphere, N_2O is destroyed by photolysis and reaction with $O(^1D)$, leading to decreasing mixing ratios with increasing potential temperature. Ozone shows a corresponding increase in the lower stratosphere. Both trace gases are used to identify the chemical tropopause[66–70]. Further, tracer-tracer correlations were used to identify mixing processes across the tropopause[67,68,71,72]. We used the N_2O-CH_4 relation as shown in the Extended Data Fig. 8. Here, N_2O is used as a stratospheric tracer, while CH_4 is used as a tropospheric tracer with sources in the ASM region. Tropospheric data

are represented by high N_2O (> 337 ppb) accompanied by high CH_4 values. Stratospheric data are represented by low N_2O (< 337 ppb) accompanied by low CH_4 values. Without recent mixing processes, the correlation of N_2O and CH_4 forms an L-shape structure[67]. With recent mixing, mixing lines between the two regimes appear[68,71]. Mixing lines in the Extended Data Fig. 8 show enhanced values of nitrate, indicating the nitrate aerosol was incorporated in the mixing process.

Calculation of required NH_4 for neutralization. We used the stoichiometric ratio of nitrate and sulfate as well as of ammonium that can neutralize these species. The concentrations of nitrate [NO_3] and sulfate [SO_4], measured by the ERICA-AMS, are taken to determine the concentration of ammonium required for neutralization [$NH_{4,req}$]:

$$[NH_{4,req}] = \frac{36}{96} \cdot [SO_4] + \frac{18}{62} \cdot [NO_3]. \quad (2)$$

The acidity or neutralization calculations take only the inorganic species into account. The calculated [$NH_{4,req}$] in comparison with the ammonium concentration measured by the ERICA-AMS provides an indication of the aerosol acidity[73]. The chloride signal is below the detection limit even after averaging over two hours. We thus excluded the chloride concentrations from the here shown analysis.

References

1. Junge, C. E., Chagnon, C. W. & Manson, J. E. A World-wide Stratospheric Aerosol Layer. *Science* **133**, 1478–1479, DOI: 10.1126/science.133.3463.1478-a (1961). https://science.sciencemag.org/content/133/3463/1478.2.full.pdf.

2. Kremser, S. *et al.* Stratospheric aerosol—Observations, processes, and impact on climate. *Rev. Geophys.* **54**, 278–335, DOI: https://doi.org/10.1002/2015RG000511 (2016). https://agupubs.onlinelibrary.wiley.com/doi/pdf/10.1002/2015RG000511.

3. Vernier, J.-P., Thomason, L. W. & Kar, J. CALIPSO detection of an Asian tropopause aerosol layer. *Geophys. Res. Lett.* **38**, DOI: https://doi.org/10.1029/2010GL046614 (2011). https://agupubs.onlinelibrary.wiley.com/doi/pdf/10.1029/2010GL046614.

4. Thomason, L. W. & Vernier, J.-P. Improved SAGE II cloud/aerosol categorization and observations of the Asian tropopause aerosol layer: 1989–2005. *Atmospheric Chem. Phys.* **13**, 4605–4616, DOI: 10.5194/acp-13-4605-2013 (2013).

5. Vernier, J.-P. *et al.* Increase in upper tropospheric and lower stratospheric aerosol levels and its potential connection with Asian pollution. *J. Geophys. Res. Atmospheres* **120**, 1608–1619, DOI: https://doi.org/10.1002/2014JD022372 (2015). https://agupubs.onlinelibrary.wiley.com/doi/pdf/10.1002/2014JD022372.

6. Höpfner, M. *et al.* Ammonium nitrate particles formed in upper troposphere from ground ammonia sources during Asian monsoons. *Nat. Geosci.* **12**, 608–612, DOI: 10.1038/s41561-019-0385-8 (2019). https://doi.org/10.1038/s41561-019-0385-8.

7. Appel, O. *et al.* Chemical analysis of the Asian tropopause aerosol layer (ATAL) with emphasis on secondary aerosol particles using aircraft-based in situ aerosol mass spectrometry. *Atmospheric Chem. Phys.* **22**, 13607–13630, DOI: 10.5194/acp-22-13607-2022 (2022).

8. Vernier, H. *et al.* Exploring the inorganic composition of the Asian Tropopause Aerosol Layer using medium-duration balloon flights. *Atmospheric Chem. Phys.* **22**, 12675–12694, DOI: 10.5194/acp-22-12675-2022 (2022).

9. Yu, P. *et al.* Abundant Nitrate and Nitric Acid Aerosol in the Upper Troposphere and Lower Stratosphere. *Geophys. Res. Lett.* **49**, e2022GL100258, DOI: https://doi.org/10.1029/2022GL100258 (2022). E2022GL100258 2022GL100258, https://agupubs.onlinelibrary.wiley.com/doi/pdf/10.1029/2022GL100258.

10. Xenofontos, C. *et al.* The impact of ammonia on particle formation in the Asian Tropopause Aerosol Layer. *npj Clim. Atmospheric Sci.* **7**, 215, DOI: 10.1038/s41612-024-00758-3 (2024).

11. Berberich, J. *et al.* Black Carbon Reflects Extremely Efficient Aerosol Wet Removal in Monsoonal Convective Transport. *Authorea Prepr.* DOI: 10.22541/essoar.172954114.48999128/v1 (2024).

12. Weigel, R. *et al.* In situ observation of new particle formation (NPF) in the tropical tropopause layer of the 2017 Asian monsoon anticyclone – Part 1: Summary of StratoClim results. *Atmospheric Chem. Phys.* **21**, 11689–11722, DOI: 10.5194/acp-21-11689-2021 (2021).

13. Mahnke, C. *et al.* The Asian tropopause aerosol layer within the 2017 monsoon anticyclone: microphysical properties derived from aircraft-borne in situ measurements. *Atmospheric Chem. Phys.* **21**, 15259–15282, DOI: 10.5194/acp-21-15259-2021 (2021).

14. Yu, P. *et al.* Efficient transport of tropospheric aerosol into the stratosphere via the Asian summer monsoon anticyclone. *Proc. Natl. Acad. Sci.* **114**, 6972–6977, DOI: 10.1073/pnas.1701170114 (2017). https://www.pnas.org/content/114/27/6972.full.pdf.

15. Fadnavis, S. *et al.* Long range transport of South and East Asian anthropogenic aerosols counteracting Arctic warming. *npj Clim. Atmospheric Sci.* **7**, 101, DOI: 10.1038/s41612-024-00633-1 (2024).

16. Graßl, S., Ritter, C., Tritscher, I. & Vogel, B. Does the Asian summer monsoon play a role in the stratospheric aerosol budget of the Arctic? *Atmospheric Chem. Phys.* **24**, 7535–7557, DOI: 10.5194/acp-24-7535-2024 (2024).

17. Solomon, S. *et al.* The role of aerosol variations in anthropogenic ozone depletion at northern midlatitudes. *J. Geophys. Res. Atmospheres* **101**, 6713–6727, DOI: https://doi.org/10.1029/95JD03353 (1996). https://agupubs.onlinelibrary.wiley.com/doi/pdf/10.1029/95JD03353.

18. Rosenlof, K. H. Changes in water vapor and aerosols and their relation to stratospheric ozone. *Comptes Rendus. Géoscience* **350**, 376–383, DOI: 10.1016/j.crte.2018.06.014 (2018).

19. Solomon, S. *et al.* The Persistently Variable "Background" Stratospheric Aerosol Layer and Global Climate Change. *Science* **333**, 866–870, DOI: 10.1126/science.1206027 (2011). https://www.science.org/doi/pdf/10.1126/science.1206027.

20. Yu, P. *et al.* Radiative forcing from anthropogenic sulfur and organic emissions reaching the stratosphere. *Geophys. Res. Lett.* **43**, 9361–9367, DOI: https://doi.org/10.1002/2016GL070153 (2016). https://agupubs.onlinelibrary.wiley.com/doi/pdf/10.1002/2016GL070153.

21. Murphy, D. M. *et al.* Radiative and chemical implications of the size and composition of aerosol particles in the existing or modified global stratosphere. *Atmospheric Chem. Phys.* **21**, 8915–8932, DOI: 10.5194/acp-21-8915-2021 (2021).

22. Hünig, A. *et al.* Design, characterization, and first field deployment of a novel aircraft-based aerosol mass spectrometer combining the laser ablation and flash vaporization techniques. *Atmospheric Meas. Tech.* **15**, 2889–2921, DOI: 10.5194/amt-15-2889-2022 (2022).

23. Lelieveld, J. *et al.* The South Asian monsoon—pollution pump and purifier. *Science* **361**, 270–273, DOI: 10.1126/science.aar2501 (2018). https://science.sciencemag.org/content/361/6399/270.full.pdf.

24. Tomsche, L. *et al.* Upper tropospheric CH_4 and CO affected by the South Asian summer monsoon during the Oxidation Mechanism Observations mission. *Atmospheric Chem. Phys.* **19**, 1915–1939, DOI: 10.5194/acp-19-1915-2019 (2019).

25. Saunois, M. *et al.* The Global Methane Budget 2000–2017. *Earth Syst. Sci. Data* **12**, 1561–1623, DOI: 10.5194/essd-12-1561-2020 (2020).

26. An, M. *et al.* Rapid increase in dichloromethane emissions from China inferred through atmospheric observations. *Nat. Commun.* **12**, 7279, DOI: 10.1038/s41467-021-27592-y (2021).

27. Pan, L. L. *et al.* East Asian summer monsoon delivers large abundances of very short-lived organic chlorine substances to the lower stratosphere. *Proc. Natl. Acad. Sci.* **121**, e2318716121, DOI: 10.1073/pnas.2318716121 (2024). https://www.pnas.org/doi/pdf/10.1073/pnas.2318716121.

28. Jöckel, P. *et al.* The atmospheric chemistry general circulation model ECHAM5/MESSy1: consistent simulation of ozone from the surface to the mesosphere. *Atmospheric Chem. Phys.* **6**, 5067–5104, DOI: 10.5194/acp-6-5067-2006 (2006).

29. Kunz, A., Konopka, P., Müller, R. & Pan, L. L. Dynamical tropopause based on isentropic potential vorticity gradients. *J. Geophys. Res. Atmospheres* **116**, DOI: https://doi.org/10.1029/2010JD014343 (2011). https://agupubs.onlinelibrary.wiley.com/doi/pdf/10.1029/2010JD014343.

30. Claxton, T. *et al.* A Synthesis Inversion to Constrain Global Emissions of Two Very Short Lived Chlorocarbons: Dichloromethane, and Perchloroethylene. *J. Geophys. Res. Atmospheres* **125**, e2019JD031818, DOI: https://doi.org/10.1029/2019JD031818 (2020). E2019JD031818 2019JD031818, https://agupubs.onlinelibrary.wiley.com/doi/pdf/10.1029/2019JD031818.

31. Ploeger, F., Konopka, P., Walker, K. & Riese, M. Quantifying pollution transport from the Asian monsoon anticyclone into the lower stratosphere. *Atmospheric Chem. Phys.* **17**, 7055–7066, DOI: 10.5194/acp-17-7055-2017 (2017).

32. Vogel, B. *et al.* Lagrangian simulations of the transport of young air masses to the top of the Asian monsoon anticyclone and into the tropical pipe. *Atmospheric Chem. Phys.* **19**, 6007–6034, DOI: 10.5194/acp-19-6007-2019 (2019).

33. Bassett, M. & Seinfeld, J. H. Atmospheric equilibrium model of sulfate and nitrate aerosols. *Atmospheric Environ. (1967)* **17**, 2237–2252, DOI: https://doi.org/10.1016/0004-6981(83)90221-4 (1983).

34. Hamill, P., Jensen, E. J., Russell, P. B. & Bauman, J. J. The Life Cycle of Stratospheric Aerosol Particles. *Bull. Am. Meteorol. Soc.* **78**, 1395 – 1410, DOI: 10.1175/1520-0477(1997)078<1395:TLCOSA>2.0.CO;2 (1997).

35. Fountoukis, C. & Nenes, A. ISORROPIA II: a computationally efficient thermodynamic equilibrium model for K^+–Ca^{2+}–Mg^{2+}–NH_4^+–Na^+–SO_4^-–NO_3^-–Cl^-–H_2O aerosols. *Atmospheric Chem. Phys.* **7**, 4639–4659, DOI: 10.5194/acp-7-4639-2007 (2007).

36. Alladi, H. K., Satheesh Chandran, P. & M, V. R. Impact of ENSO on the UTLS chemical composition in the Asian Summer Monsoon Anticyclone. *Atmospheric Res.* **309**, 107551, DOI: https://doi.org/10.1016/j.atmosres.2024.107551 (2024).

37. Katich, J. M. *et al.* Pyrocumulonimbus affect average stratospheric aerosol composition. *Science* **379**, 815–820, DOI: 10.1126/science.add3101 (2023). https://www.science.org/doi/pdf/10.1126/science.add3101.

38. Ma, C. *et al.* Smoke-charged vortex doubles hemispheric aerosol in the middle stratosphere and buffers ozone depletion. *Sci. Adv.* **10**, eadn3657, DOI: 10.1126/sciadv.adn3657 (2024). https://www.science.org/doi/pdf/10.1126/sciadv.adn3657.

39. Froyd, K. D. *et al.* Aerosol composition of the tropical upper troposphere. *Atmospheric Chem. Phys.* **9**, 4363–4385, DOI: 10.5194/acp-9-4363-2009 (2009).

40. Schulz, C. *et al.* Aircraft-based observations of isoprene-epoxydiol-derived secondary organic aerosol (IEPOX-SOA) in the tropical upper troposphere over the Amazon region. *Atmospheric Chem. Phys.* **18**, 14979–15001, DOI: 10.5194/acp-18-14979-2018 (2018).

41. Martinsson, B. G. *et al.* Formation and composition of the UTLS aerosol. *npj Clim. Atmospheric Sci.* **2**, 40, DOI: 10.1038/s41612-019-0097-1 (2019).

42. Solomon, S. *et al.* Monsoon circulations and tropical heterogeneous chlorine chemistry in the stratosphere. *Geophys. Res. Lett.* **43**, 12,624–12,633, DOI: https://doi.org/10.1002/2016GL071778 (2016). https://agupubs.onlinelibrary.wiley.com/doi/pdf/10.1002/2016GL071778.

43. Strahan, S. E. *et al.* Unexpected Repartitioning of Stratospheric Inorganic Chlorine After the 2020 Australian Wildfires. *Geophys. Res. Lett.* **49**, e2022GL098290, DOI: https://doi.org/10.1029/2022GL098290 (2022). E2022GL098290 2022GL098290, https://agupubs.onlinelibrary.wiley.com/doi/pdf/10.1029/2022GL098290.

44. Zhu, Y. *et al.* Evaluating the Importance of Nitrate-Containing Aerosols for the Asian Tropopause Aerosol Layer. *J. Geophys. Res. Atmospheres* **129**, e2024JD041283, DOI: https://doi.org/10.1029/2024JD041283 (2024). E2024JD041283 2024JD041283, https://agupubs.onlinelibrary.wiley.com/doi/pdf/10.1029/2024JD041283.

45. Keith, D. W., Weisenstein, D. K., Dykema, J. A. & Keutsch, F. N. Stratospheric solar geoengineering without ozone loss. *Proc. Natl. Acad. Sci.* **113**, 14910–14914, DOI: 10.1073/pnas.1615572113 (2016). https://www.pnas.org/doi/pdf/10.1073/pnas.1615572113.

46. Solomon, S. *et al.* Chlorine activation and enhanced ozone depletion induced by wildfire aerosol. *Nature* **615**, 259–264, DOI: 10.1038/s41586-022-05683-0 (2023).

47. Adcock, K. E. *et al.* Aircraft-Based Observations of Ozone-Depleting Substances in the Upper Troposphere and Lower Stratosphere in and Above the Asian Summer Monsoon. *J. Geophys. Res. Atmospheres* **126**, e2020JD033137, DOI: https://doi.org/10.1029/2020JD033137 (2021). E2020JD033137 2020JD033137, https://agupubs.onlinelibrary.wiley.com/doi/pdf/10.1029/2020JD033137.

48. Borrmann, S. *et al.* Heterogeneous reactions on stratospheric background aerosols, volcanic sulfuric acid droplets, and type I polar stratospheric clouds: Effects of temperature fluctuations and differences in particle phase. *J. Geophys. Res. Atmospheres* **102**, 3639–3648, DOI: https://doi.org/10.1029/96JD02976 (1997). https://agupubs.onlinelibrary.wiley.com/doi/pdf/10.1029/96JD02976.

49. Mu, Q. *et al.* Temperature effect on phase state and reactivity controls atmospheric multiphase chemistry and transport of PAHs. *Sci. Adv.* **4**, eaap7314, DOI: 10.1126/sciadv.aap7314 (2018). https://www.science.org/doi/pdf/10.1126/sciadv.aap7314.

50. Tritscher, I. *et al.* Polar stratospheric clouds: Satellite observations, processes, and role in ozone depletion. *Rev. Geophys.* **59**, e2020RG000702, DOI: https://doi.org/10.1029/2020RG000702 (2021). E2020RG000702 2020RG000702, https://agupubs.onlinelibrary.wiley.com/doi/pdf/10.1029/2020RG000702.

51. Wagner, R. *et al.* Solid Ammonium Nitrate Aerosols as Efficient Ice Nucleating Particles at Cirrus Temperatures. *J. Geophys. Res. Atmospheres* **125**, e2019JD032248, DOI: https://doi.org/10.1029/2019JD032248 (2020). E2019JD032248 2019JD032248, https://agupubs.onlinelibrary.wiley.com/doi/pdf/10.1029/2019JD032248.

52. Suess, D. T. & Prather, K. A. Mass Spectrometry of Aerosols. *Chem. Rev.* **99**, 3007–3036, DOI: 10.1021/cr980138o (1999).

53. Drewnick, F. *et al.* A new time-of-flight aerosol mass spectrometer (TOF-AMS)—instrument description and first field deployment. *Aerosol Sci. Technol.* **39**, 637–658, DOI: 10.1080/02786820500182040 (2005). https://doi.org/10.1080/02786820500182040.

54. Canagaratna, M. *et al.* Chemical and microphysical characterization of ambient aerosols with the aerodyne aerosol mass spectrometer. *Mass Spectrom. Rev.* **26**, 185–222, DOI: https://doi.org/10.1002/mas.20115 (2007). https://analyticalsciencejournals.onlinelibrary.wiley.com/doi/pdf/10.1002/mas.20115.

55. Friedl-Vallon, F. *et al.* Instrument concept of the imaging Fourier transform spectrometer GLORIA. *Atmospheric Meas. Tech.* **7**, 3565–3577, DOI: 10.5194/amt-7-3565-2014 (2014).

56. Riese, M. *et al.* Gimballed Limb Observer for Radiance Imaging of the Atmosphere (GLORIA) scientific objectives. *Atmospheric Meas. Tech.* **7**, 1915–1928, DOI: 10.5194/amt-7-1915-2014 (2014).

57. Kleinert, A. *et al.* Level 0 to 1 processing of the imaging Fourier transform spectrometer GLORIA: generation of radiometrically and spectrally calibrated spectra. *Atmospheric Meas. Tech.* **7**, 4167–4184, DOI: 10.5194/amt-7-4167-2014 (2014).

58. Ungermann, J. *et al.* Quantification and mitigation of the instrument effects and uncertainties of the airborne limb imaging FTIR GLORIA. *Atmospheric Meas. Tech.* **15**, 2503–2530, DOI: 10.5194/amt-15-2503-2022 (2022).

59. Johansson, S. *et al.* Airborne limb-imaging measurements of temperature, HNO_3, O_3, $ClONO_2$, H_2O and CFC-12 during the Arctic winter 2015/2016: characterization, in situ validation and comparison to Aura/MLS. *Atmospheric Meas. Tech.* **11**, 4737–4756, DOI: 10.5194/amt-11-4737-2018 (2018).

60. McManus, J. B. *et al.* Application of quantum cascade lasers to high-precision atmospheric trace gas measurements. *Opt. Eng.* **49**, 111124, DOI: 10.1117/1.3498782 (2010).

61. Hersbach, H. *et al.* The ERA5 global reanalysis. *Q. J. Royal Meteorol. Soc.* **146**, 1999–2049, DOI: https://doi.org/10.1002/qj.3803 (2020).

62. McIntyre, M. E. & Palmer, T. N. Breaking planetary waves in the stratosphere. *Nature* **305**, 593–600, DOI: 10.1038/305593a0 (1983).

63. McDuffie, E. E. *et al.* A global anthropogenic emission inventory of atmospheric pollutants from sector- and fuel-specific sources (1970–2017): an application of the Community Emissions Data System (CEDS). *Earth Syst. Sci. Data* **12**, 3413–3442, DOI: 10.5194/essd-12-3413-2020 (2020).

64. Pringle, K. J. *et al.* Description and evaluation of GMXe: a new aerosol submodel for global simulations (v1). *Geosci. Model. Dev.* **3**, 391–412, DOI: 10.5194/gmd-3-391-2010 (2010).

65. Lauther, V. *et al.* In situ observations of CH_2Cl_2 and $CHCl_3$ show efficient transport pathways for very short-lived species into the lower stratosphere via the Asian and the North American summer monsoon. *Atmospheric Chem. Phys.* **22**, 2049–2077, DOI: 10.5194/acp-22-2049-2022 (2022).

66. Zahn, A. & Brenninkmeijer, C. A. New Directions: A Chemical Tropopause Defined. *Atmospheric Environ.* **37**, 439–440, DOI: https://doi.org/10.1016/S1352-2310(02)00901-9 (2003).

67. Fischer, H. *et al.* Tracer correlations in the northern high latitude lowermost stratosphere: Influence of cross-tropopause mass exchange. *Geophys. Res. Lett.* **27**, 97–100, DOI: https://doi.org/10.1029/1999GL010879 (2000). https://agupubs.onlinelibrary.wiley.com/doi/pdf/10.1029/1999GL010879.

68. Hoor, P., Fischer, H., Lange, L., Lelieveld, J. & Brunner, D. Seasonal variations of a mixing layer in the lowermost stratosphere as identified by the CO-O3 correlation from in situ measurements. *J. Geophys. Res. Atmospheres* **107**, ACL 1–1–ACL 1–11, DOI: https://doi.org/10.1029/2000JD000289 (2002). https://agupubs.onlinelibrary.wiley.com/doi/pdf/10.1029/2000JD000289.

69. Pan, L. L., Randel, W. J., Gary, B. L., Mahoney, M. J. & Hintsa, E. J. Definitions and sharpness of the extratropical tropopause: A trace gas perspective. *J. Geophys. Res. Atmospheres* **109**, DOI: https://doi.org/10.1029/2004JD004982 (2004). https://agupubs.onlinelibrary.wiley.com/doi/pdf/10.1029/2004JD004982.

70. Hegglin, M. I. *et al.* Measurements of NO, NO_y, N_2O, and O_3 during SPURT: implications for transport and chemistry in the lowermost stratosphere. *Atmospheric Chem. Phys.* **6**, 1331–1350, DOI: 10.5194/acp-6-1331-2006 (2006).

71. Müller, S. *et al.* Impact of the Asian monsoon on the extratropical lower stratosphere: trace gas observations during TACTS over Europe 2012. *Atmospheric Chem. Phys.* **16**, 10573–10589, DOI: 10.5194/acp-16-10573-2016 (2016).

72. Krause, J. *et al.* Mixing and ageing in the polar lower stratosphere in winter 2015–2016. *Atmospheric Chem. Phys.* **18**, 6057–6073, DOI: 10.5194/acp-18-6057-2018 (2018).

73. Zhang, Q., Jimenez, J. L., Worsnop, D. R. & Canagaratna, M. A Case Study of Urban Particle Acidity and Its Influence on Secondary Organic Aerosol. *Environ. Sci. & Technol.* **41**, 3213–3219, DOI: 10.1021/es061812j (2007). PMID: 17539528, https://doi.org/10.1021/es061812j.

Acknowledgements

We thank the German Aerospace Center Flight Experiments (DLR-FX) facility for campaign support and organization as well as for operating HALO. Special thanks to the pilots, engineers, technicians and the operations team. We also acknwoledge the BAHAMAS team (DLR-FX) for operating the basic sensor system on HALO and providing data. The authors would also like to thank the flight planning team, in particular Felix Plöger, Jens-Uwe Grooß, Christian Rolf, Rolf Müller, and Bärbel Vogel. We would also thank the enviscope team of Rolf Maser for their technical support during the campaign. The PHILEAS mission was funded by the Deutsche Forschungsgemeinschaft (DFG, German Research Foundation) (HALO-SPP 1294, project no: 461449927, HO 4225/17-1). The funding for individual projects within PHILEAS was provided by the DFG (KO 6470/1-1, HO 4225/19-1, HO 4120/4-1, VO 1530/9-1). The study was supported by TRR 301 "TPChange" (Project-ID 428312742). This research has received support from the Max Planck Society (MPG) and the Max Planck Graduate Centre (MPGC). The design and construction of the ERICA instrument was financed by the FP7/2013-2019 ERC Advanced Research Grant "EXCATRO" (grant no. 321040). Jörn Ungermann, Sören Johansson, and Michael Höpfner received support from the ESA CARITEX project (4000141036/23/NL/FF/ab). Laura Tomsche will acknowledge the support by the project MEFKON (20F2202B) funded by the German Federal Ministry for Economic Affairs and Climate Action within LuFo 6-3. We thank the MPI-C for support, particularly the mechanical and electronics workshop, the Department of Climate Geochemistry as well as the Graphic office. We thank Johannes Lucke (DLR) for providing the cloud flag data from the Backscatter Cloud Probe with Polarization Detection (BCPD). The authors further acknowledge the scientific discussions with Philipp Joppe.

Author contributions statement

P.H. and M.R. designed the PHILEAS research project. F.E., O.E., J.S., A.D., S.M., P.B., and F.K. carried out the ERICA measurements. F.E. and O.E. with the help of O.A. and F.K. generated the final ERICA data set. F.K. with the help of F.E., O.E., O.A., and J.S. analyzed the ERICA data. M.K. and A.P. provided the EMAC data. V.L. and C.M.V. provided the HAGAR-V data. P.H., L.O., N.E., F.W., H.C.L., D.K., and H.B. provided the UMAQS data. H.C.L. provided the ERA5 data. S.J., J.U., M.H., and E.K. provided the GLORIA data. A.Z. provided the FAIRO data. L.T. operated the BCPD instrument. P.H., S.B., J.S., M.K., and F.K. contributed to the flight planning, data interpretation, and/or scientific discussion. F.K. wrote the manuscript with assistance from all authors.

Additional information

The authors declare no competing interests.

S1 Isokinetic aerosol sampling

The aerosol sampling was conducted with the HALO aerosol submicrometer inlet (HASI). The inlet was first described in Andreae et al.[1]. The HASI is mounted on top of the fuselage outside of the aircraft boundary layer. The sampled air is divided over four sampling lines. During PHILEAS, these lines were used by the ERICA instrument, the FASD instrument, and as a bypass line. One sample line was not in use and thus closed with a blind plug. The HASI flow control unit (FCU) aims to regulate the sample airflow in each of the four lines to achieve near-isokinetic sampling (up to particle diameters of 2-3 µm) according to the actual speed of the aircraft and ambient air density. The ERICA instrument was connected to the HASI via a 1/4 inch stainless steel tubing.

S2 Signal processing and data analysis for the ERICA-AMS

The ERICA instrument is decribed in detail in Hünig et al.[2], Dragoneas et al.[3], and Molleker et al.[4]. The signal preparation and analysis was conducted similar to how it is described in the Supplementary of Appel et al.[5] with minor changes. We used the software TofWare 2.5.7 and adjusted the settings to comply with the ERICA-AMS data. For this study, we have in total 27448 data points after excluding data collected during particle filter, during cloud passes, collected below 8 km, and during BB events. Each data point is representative for 10 s, resulting in a total sampling time of 76 h and 15 min over all 11 research flights conducted out of Anchorage. In the following, we only describe the differences in the data post-processing between StratoClim 2017 and PHILEAS 2023.

We conducted four zeroing measurements for each flight. This was obtained by using a three-way valve system. The bypass line was equipped with a particle filter for zeroing measurements. The valve system was manually switched between filter and sample mode. One zeroing measurement was taken immediately before taxiing (after 4 h of pumping to achieve a good vacuum). Two zeroing measurements were conducted during the flight, and one after landing. Each zeroing measurement phase took 5 min. During the data post-processing, those filter measurements were taken to adjust the fragmentation table[6]. Further, the air beam into the vacuum was reduced by a smaller skimmer diameter behind the lens (from 1.9 mm to 1 mm). With this adjustment, we could determine the ammonium signal as it is generally recommended with the m/z 16 and 17 signal according to Allan et. al[6]. Moreover, the organic signal at m/z 29 was determined according to the fragmentation table in Allan et al.[6].

The conversion of the measured signal into a mass concentration requires the so-called ionization efficiency (IE) calibration. We used the mass-based method[7]. Details of the calibration procedure can be found in Appel et al.[5]. We conducted five IE calibrations during the measurement phase in Anchorage. Based on the air beam signal during zeroing measurements, we determined the appropriate calibration for each flight. We achieved different calibration values compared to StratoClim 2017 due to several adjustments and tuning of the high voltages.

S3 Detection limits

A shutter in front of the ERICA-AMS ionization region determines if ambient air (including aerosol) is blocked (closed) or reaching the ionization region (open). One measurement cycle of the ERICA-AMS consists of 10 s or 25 raw spectra. When the shutter is open, 11 raw spectra (within 4.4 s) are taken, which are representative for the ambient aerosol measurements. When the shutter is closed, 11 raw spectra (within 4.4 s) are taken, which are representative for the background measurements (i.e. residual vacuum signal). Three raw spectra (1.2 s) are discarded because of the shutter switching. The detection limits (DL) of nitrate, ammonium, sulfate, and organic matter are determined by analysing the noise of the background measurement when the shutter is closed[8]. The DL is given as 3·sigma. A Savitzki-Golay filter[9] has been implemented to separate statistical noise from background trends due to improving vacuum and varying temperatures during the flight. For further details see Supplementary of Appel et al.[5]. Figure S1 displays the DL for all species in each bin of potential temperature.

S4 Model evaluation

EMAC model results were evaluated with observations from the PHILEAS 2023 aircraft missions (Fig. S2). Simulated ammonium and nitrate resemble the observed patterns, with increasing concentrations in the lower stratosphere. Note, all flight tracks that are taken here are not filtered by ASM-influenced air. Sulfate concentrations are underestimated in the free troposphere, but agree with observations in the lower stratosphere. The overestimation of organic compounds in the lower stratosphere can be attributed to missing photochemical sinks of semi- and low-volatile organic species in the stratosphere in the EMAC model, leading to an accumulation of organic compounds. Thus, we do not perform organic modelling studies in the manuscript.

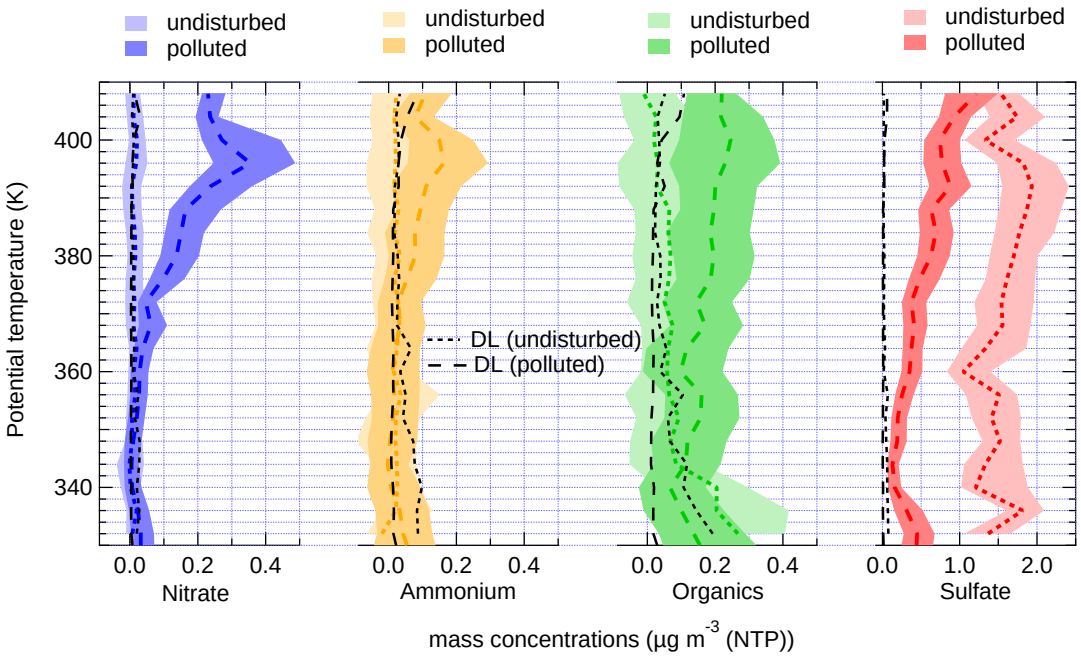

Figure S1. ERICA-AMS mass concentrations of particulate nitrate (blue), ammonium (orange), organics (green), and sulfate (red) as a function of potential temperature. The thick lines and the shaded areas represent the medians and interquartile range, respectively, in the corresponding potential temperature bin. Data associated with undisturbed stratospheric and polluted air given in lighter and darker colours, respectively. Black dotted and dashed lines show the detection limits (DL) of data associated with undisturbed stratospheric and polluted air, respectively. The DL is displayed for each potential temperature bin.

A similar model setup was evaluated with observations from the StratoClim 2017 aircraft mission elsewhere[10]. Ammonium, nitrate, and organic aerosol show a maximum between 16 km and 18 km in both, the simulation and observations of the StratoClim campaign. The ammonium nitrate maximum is slightly underestimated by the model, most likely due to flight sampling and the limited model resolution. Overall, EMAC simulations show reasonable agreement with observations for ammonium, nitrate, and sulfate in the UTLS, justifying model studies on the transport and persistence of ASM-influenced air.

S5 Model sensitivity studies

The reference EMAC simulation used for the evaluation (see previous section) and the model results are performed using baseline anthropogenic emissions from the CEDS emission database[11]. Focusing on the UTLS region, our simulations reproduce the observed concentrations and processes reasonably well. In addition, we performed sensitivity studies without combined anthropogenic land emissions of sulfur dioxide (SO_2), ammonia (NH_3), and nitrogen oxides (NO_x) from South and East Asia, and excluding each emission flux independently. Figure S3 exemplary shows ammonia land emissions in the reference and sensitivity simulation (with excluded emissions from South and East Asia).

The sensitivity studies showed that the enhanced ammonium nitrate can almost exclusively be attributed to emissions uplifted from South and East Asia during the monsoon season. Further, removing the emissions fluxes separately revealed that ammonia emissions mostly control UTLS ammonium nitrate concentrations in the ATAL (in agreement with the findings of Xenofontos et al.[10]) and in the ExLS.

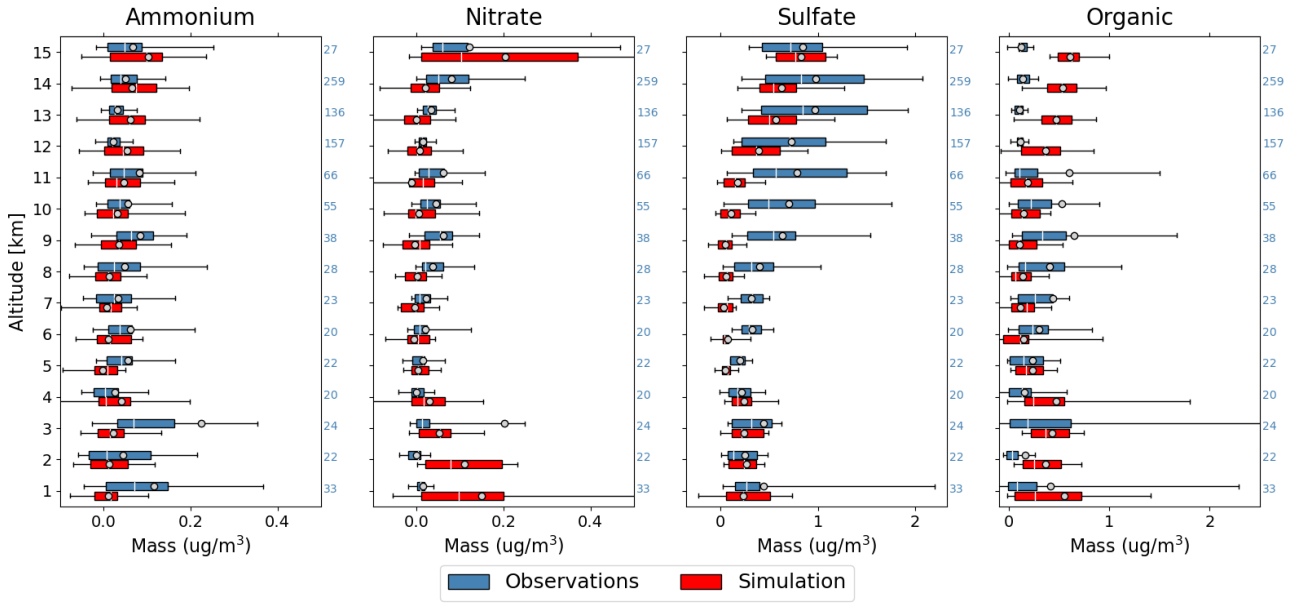

Figure S2. Comparison of observed and EMAC-simulated aerosol concentrations during the PHILEAS aircraft mission. Model output was sampled along the flight tracks. The Box-Whisker plots show the median (white line), mean (grey circle), interquartile range (box), and the 5% and 95% percentile.

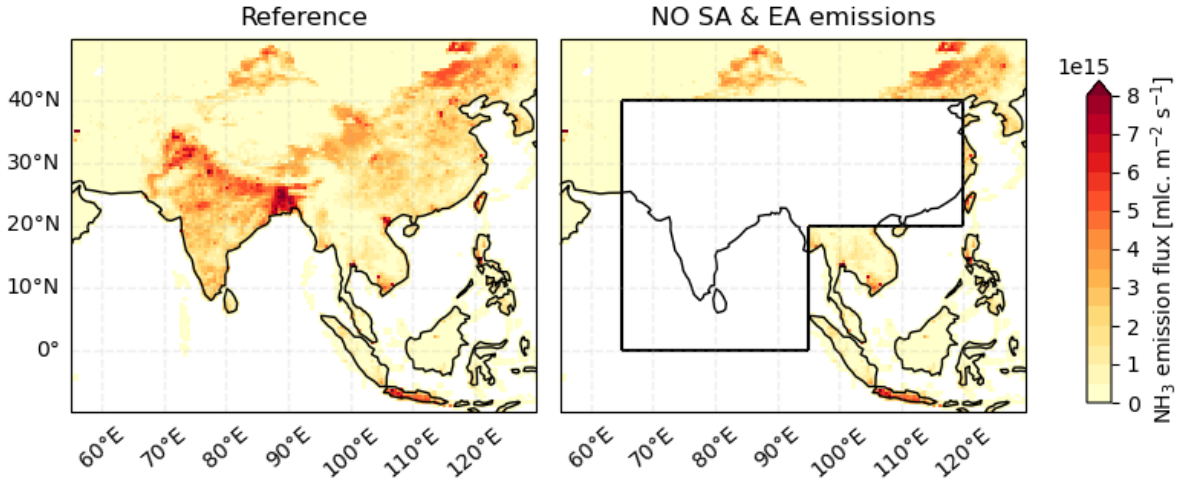

Figure S3. Ammonia (NH_3) emissions in the numerical simulations with EMAC. White areas indicate zero NH_3 emissions. In the reference simulation (left) South Asian emissions dominate the Asian contribution. In the sensitivity study anthropogenic NH_3 (and other species, see text) emissions from South Asia (SA) and East Asia (EA) were excluded (box).

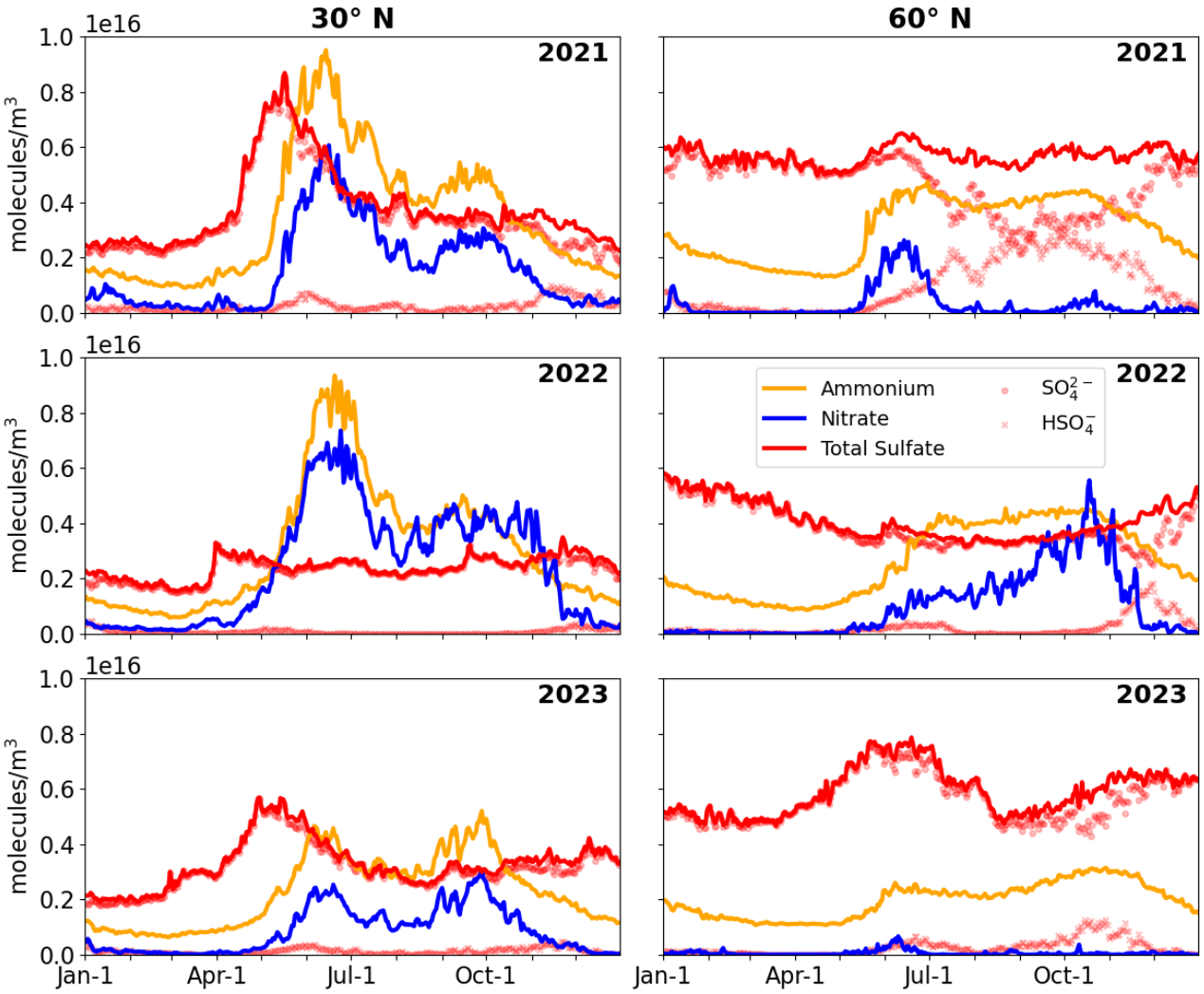

Figure S4. EMAC simulated timeline of zonally averaged inorganic aerosol concentrations between 370 and 390 K at 30° N (left; ATAL region) and 60° N (right; showing the ASM outflow) latitude. Total sulfate concentrations are displayed (red), consisting of the contribution of bisulfate (HSO_4^-; red crosses) and the remaining sulfate (SO_4^{2-}; red circles). Bisulfate forms in the transition between ammonia-rich to ammonia-poor conditions, according to the model results. The years 2023 and 2021 were influenced by increased volcanic activity. In 2023, the ATAL was weaker than in the previous years.

References

1. Andreae, M. O. *et al.* Aerosol characteristics and particle production in the upper troposphere over the Amazon Basin. *Atmospheric Chem. Phys.* **18**, 921–961, DOI: 10.5194/acp-18-921-2018 (2018).

2. Hünig, A. *et al.* Design, characterization, and first field deployment of a novel aircraft-based aerosol mass spectrometer combining the laser ablation and flash vaporization techniques. *Atmospheric Meas. Tech.* **15**, 2889–2921, DOI: 10.5194/amt-15-2889-2022 (2022).

3. Dragoneas, A. *et al.* The realization of autonomous, aircraft-based, real-time aerosol mass spectrometry in the upper troposphere and lower stratosphere. *Atmospheric Meas. Tech.* **15**, 5719–5742, DOI: 10.5194/amt-15-5719-2022 (2022).

4. Molleker, S. *et al.* Application of an O-ring pinch device as a constant-pressure inlet (CPI) for airborne sampling. *Atmospheric Meas. Tech.* **13**, 3651–3660, DOI: 10.5194/amt-13-3651-2020 (2020).

5. Appel, O. *et al.* Chemical analysis of the Asian tropopause aerosol layer (ATAL) with emphasis on secondary aerosol particles using aircraft-based in situ aerosol mass spectrometry. *Atmospheric Chem. Phys.* **22**, 13607–13630, DOI: 10.5194/acp-22-13607-2022 (2022).

6. Allan, J. D. *et al.* A generalised method for the extraction of chemically resolved mass spectra from Aerodyne aerosol mass spectrometer data. *J. Aerosol Sci.* **35**, 909–922, DOI: 10.1016/j.jaerosci.2004.02.007 (2004).

7. Drewnick, F. *et al.* A New Time-of-Flight Aerosol Mass Spectrometer (TOF-AMS)—Instrument Description and First Field Deployment. *Aerosol Sci. Technol.* **39**, 637–658, DOI: 10.1080/02786820500182040 (2005). https://doi.org/10.1080/02786820500182040.

8. Drewnick, F., Hings, S. S., Alfarra, M. R., Prevot, A. S. H. & Borrmann, S. Aerosol quantification with the Aerodyne Aerosol Mass Spectrometer: detection limits and ionizer background effects. *Atmospheric Meas. Tech.* **2**, 33–46, DOI: 10.5194/amt-2-33-2009 (2009).

9. Savitzky, A. & Golay, M. J. E. Smoothing and Differentiation of Data by Simplified Least Squares Procedures. *Anal. Chem.* **36**, 1627–1639, DOI: 10.1021/ac60214a047 (1964). https://doi.org/10.1021/ac60214a047.

10. Xenofontos, C. *et al.* The impact of ammonia on particle formation in the Asian Tropopause Aerosol Layer. *npj Clim. Atmospheric Sci.* **7**, 215, DOI: 10.1038/s41612-024-00758-3 (2024).

11. McDuffie, E. E. *et al.* A global anthropogenic emission inventory of atmospheric pollutants from sector- and fuel-specific sources (1970–2017): an application of the Community Emissions Data System (CEDS). *Earth Syst. Sci. Data* **12**, 3413–3442, DOI: 10.5194/essd-12-3413-2020 (2020).

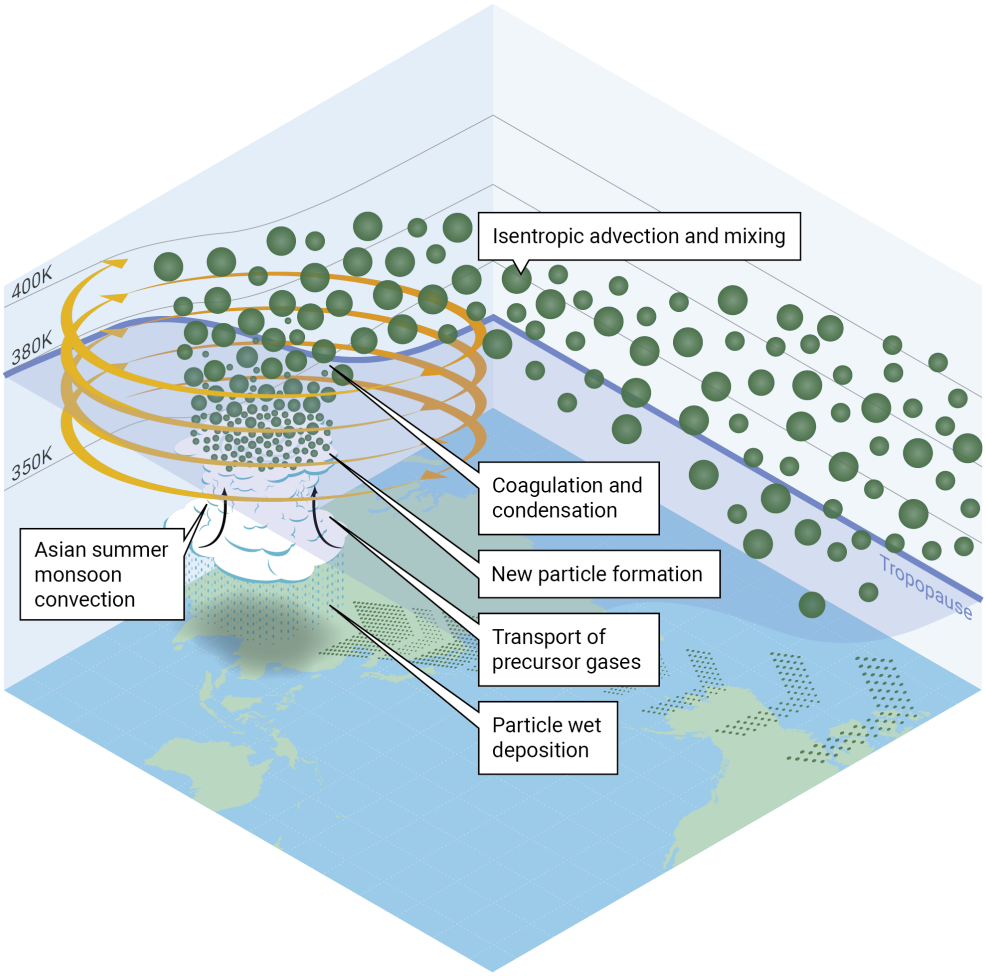

Extended Data Fig. 5. Schematic of the formation and transport processes of ASM aerosol. Transport of precursor gases from the Asian boundary layer into the upper troposphere driven by the ASM. Efficient aerosol wet deposition in the ASM convective transport. Formation of the ATAL by gas-to-particle conversion (i.e. new particle formation and subsequent particle growth by coagulation and condensation) within the slow diabatic uplift in the isolated system of the ASM anticyclone. Northward transport into the ExLS driven by isentropic advection and mixing above 370 K potential temperature.

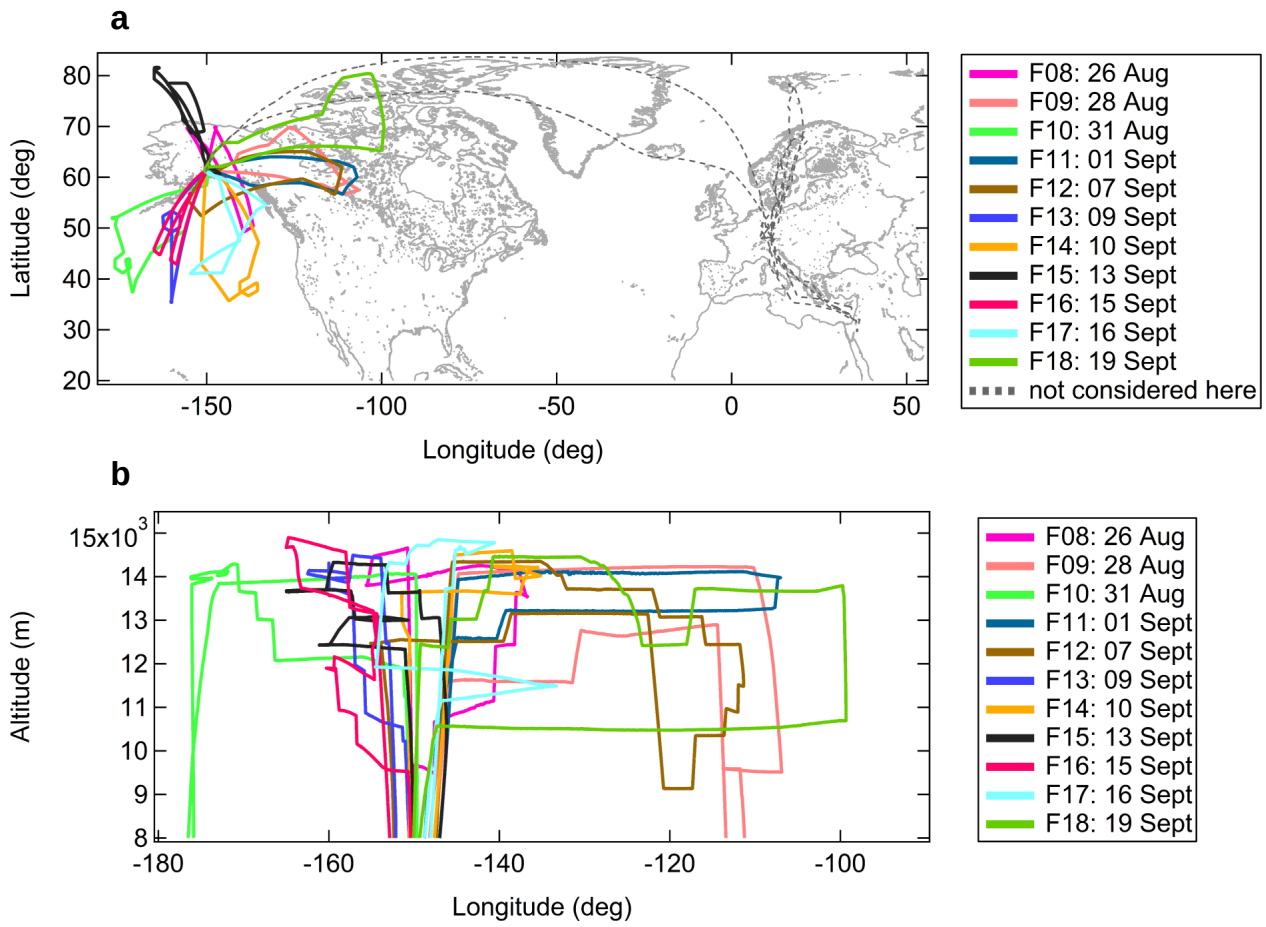

Extended Data Fig. 6. Overview of flight tracks. Flight tracks of the eleven research flights conducted from Anchorage during the PHILEAS mission in August and September 2023 **a,** on a map showing the Northern hemisphere and **b,** as a function of altitude and longitude. Different colours show individual flights. Dashed grey lines show flight tracks out of Oberpfaffenhofen, which were not considered for this study.

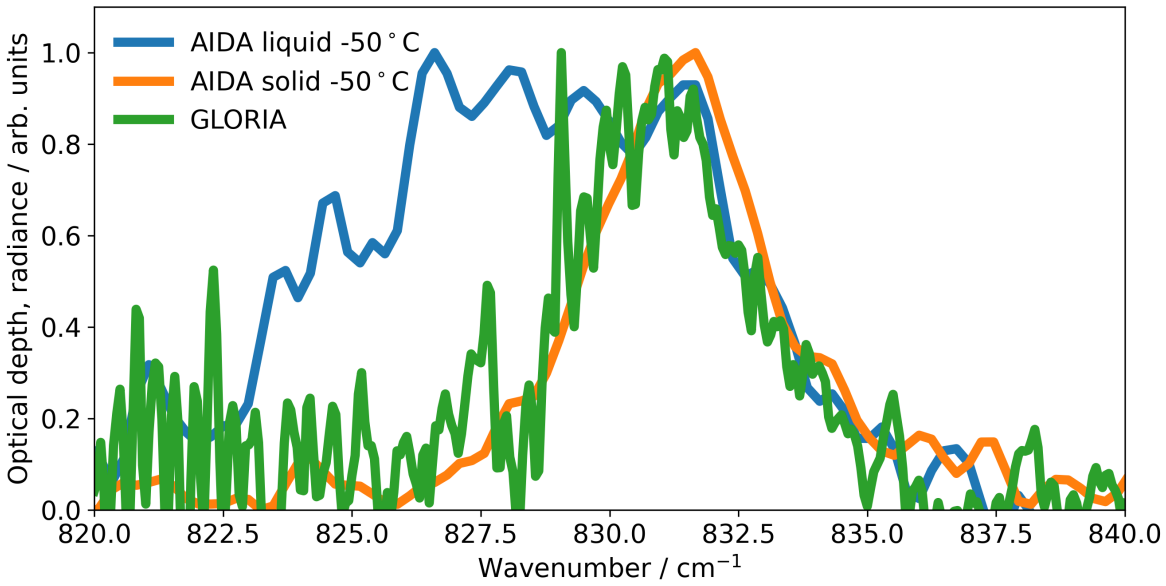

Extended Data Fig. 7. Infrared spectra of AN measured by GLORIA. Laboratory (AIDA) measurements of liquid and solid AN, as shown in Supplementary Figure 1 of Höpfner et al.[6], together with GLORIA measurements of PHILEAS research flight on September 1, 2023 (as shown in Fig. 1b). GLORIA spectra with 0.0625 cm^{-1} spectral resolution have been averaged at altitudes of 13.5-14.0 km for times with and without measurements of AN (2:41-2:55 UTC and 2:59-3:13 UTC, respectively). Normalized differences between these averages are shown as the green line.

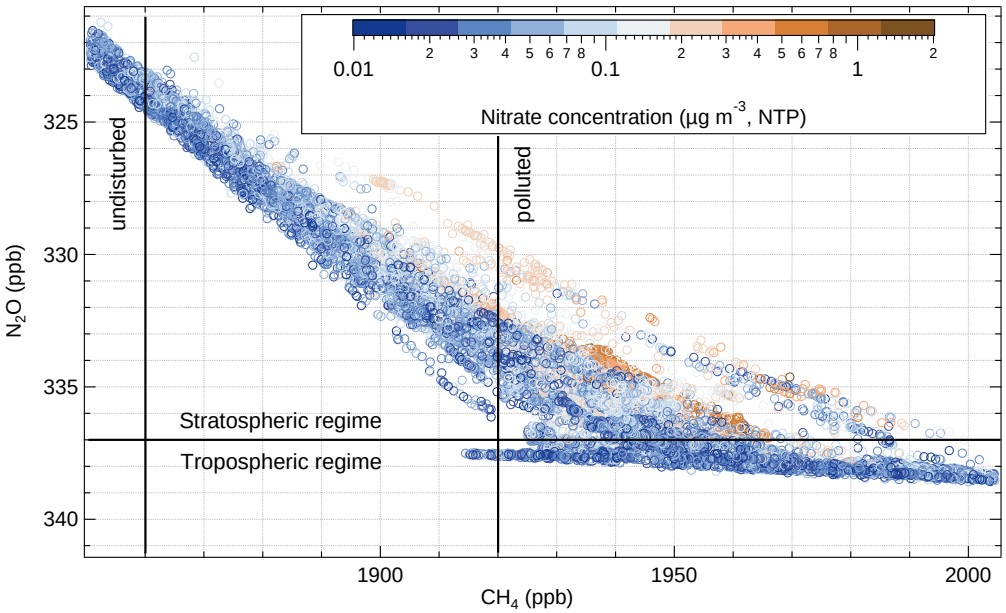

Extended Data Fig. 8. N_2O-CH_4-correlation measured by UMAQS with coloured nitrate concentration from the ERICA-AMS. The N_2O value of 337 ppb separates the tropospheric from the stratospheric regime, indicated by a horizontal black line. The CH_4 values of 1920 ppb and 1860 ppb separate the polluted from the undisturbed stratospheric regime, indicated by vertical black lines. Enhanced concentrations of nitrate are abundant on intermediate (mixing) lines between the tropospheric and stratospheric regimes.

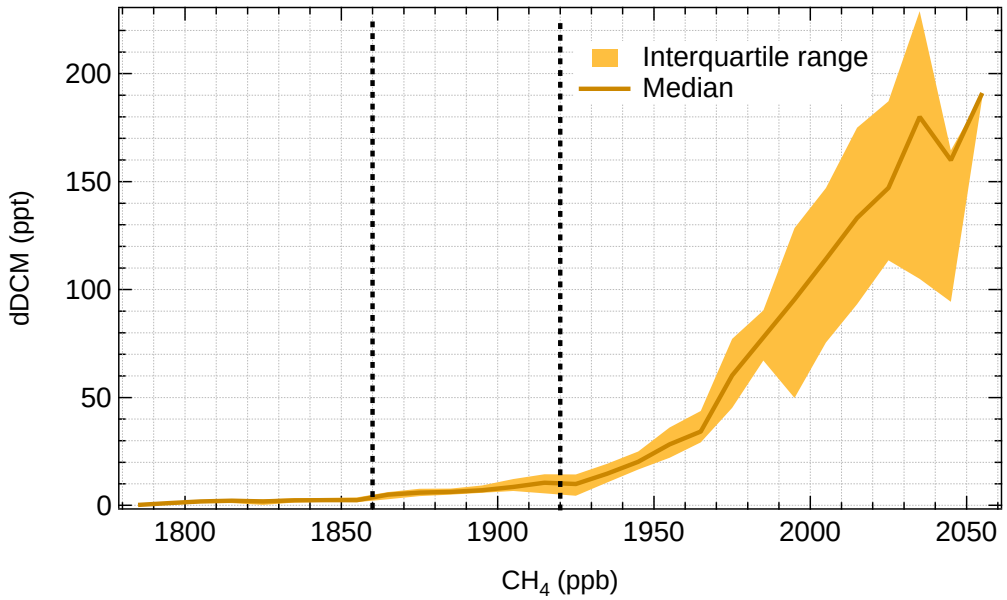

Extended Data Fig. 9. Comparison between dDCM (delta dichloromethane) and methane (CH_4). The thick line and the shaded area represent the medians and interquartile ranges, respectively, in the corresponding CH_4-bin. The dashed lines show the CH_4 thresholds (1860 ppb and 1920 ppb).